Published in final edited form as:
Neuroimage. 2013 September ; 78: 385–395. doi:10.1016/j.neuroimage.2013.04.045.

Characterization of non-hemodynamic functional signal measured by spin-lock fMRI

Tao Jin and **Seong-Gi Kim**
Neuroimaging Laboratory, Department of Radiology, University of Pittsburgh, Pittsburgh, PA, 15203

Abstract

Current functional MRI techniques measure hemodynamic changes induced by neural activity. Alternative measurement of signals originated from tissue is desirable and may be achieved using $T_1\rho$, the spin-lattice relaxation time in the rotating-frame, which is measured by spin-lock MRI. Functional $T_1\rho$ changes in the brain can have contributions from vascular dilation, tissue acidosis, and potentially other contributions. When the blood contributions were suppressed with a contrast agent at 9.4 T, a small tissue-originated $T_1\rho$ change was consistently observed at the middle cortical layers of cat visual cortex during visual stimulation, which had different dynamic characteristics compared to hemodynamic fMRI such as a faster response and no post-stimulus undershoot. Functional tissue $T_1\rho$ is highly dependent on the magnetic field strength and experimental parameters such as the power of the spin-locking pulse. With a 500 Hz spin-locking pulse, the tissue $T_1\rho$ without the blood contribution increased during visual stimulation, but decreased during acidosis-inducing hypercapnia and global ischemia, indicating different signal origins. Phantom studies suggest that it may have contribution from concentration decrease in metabolites. Even though the sensitivity is much weaker than BOLD and its exact interpretation needs further investigation, our results show that non-hemodynamic functional signal can be consistently observed by spin-lock fMRI.

Keywords

tissue-specific; functional MRI; non-hemodynamics; spin-lock; metabolism

Introduction

The ability of functional magnetic resonance imaging (fMRI) to detect brain function noninvasively with high spatial resolution opens great opportunities to advance our understanding of brain organization and function, and may potentially provide new methods to help the diagnosis and treatment of neurological diseases. Elevated neuronal activity increases oxygen and glucose metabolism in tissue and modulates hemodynamics including blood flow, volume and oxygenation level. Currently, almost all fMRI techniques are based on hemodynamic responses thus their spatial and temporal resolutions are intrinsically limited by vasculature density and regulation (Kim and Ogawa, 2012). Moreover, the exact

Corresponding authors: Tao Jin taj6@pitt.edu Seong-Gi Kim kimsg@pitt.edu Address: 3025 E Carson Street Room 156 Department of Radiology University of Pittsburgh PA, 15203.

correlation between hemodynamic-based fMRI and neuronal activation is still not fully understood and remains a concern for many neuroscientists (Editorial, 2009). There has been wide interest to investigate tissue-originated fMRI signals that are not based on hemodynamics and have closer correlation with the neuronal activities. However, despite some encouraging results in phantom, *in vitro* and non-brain studies, *in vivo* brain imaging of neuronal activity directly or a change in neuronal cell microstructure has been challenging, and the robustness of detection is also controversial (Bandettini et al., 2005; Chu et al., 2004; Jin and Kim, 2008b; Le Bihan et al., 2006; Miller et al., 2007; Park et al., 2004; Parkes et al., 2007; Tang et al., 2008; Truong and Song, 2006; Xiong et al., 2003).

Functional changes in the brain tissue microenvironment/microstructure may be detected with a $T_1\rho$ contrast. When a B_1 spin-locking (SL) pulse is applied along the direction of transverse magnetization immediately after a non-selective 90° excitation on the resonance frequency of water, the magnetization is "locked" by the B_1 pulse and decays with a time constant $T_1\rho$, which is named as the spin-lattice relaxation time in the rotating-frame. The nutation frequency of the SL pulse, $\omega_1 = \gamma B_1$, is usually several kHz or less for *in vivo* studies, and $T_1\rho$ relaxation is sensitive to the water fluctuations caused by physical processes with correlation time τ close to $1/2\pi\omega_1$. Recent studies have demonstrated that proton exchange between bulk water and labile protons of protein or metabolites is an important contributor for the low-frequency $T_1\rho$ dispersion (the dependency of $T_1\rho$ on ω_1) in biological tissue (Duvvuri et al., 2001; Jin et al., 2011; Makela et al., 2001). Due to its sensitiveness to the local tissue microenvironment and microstructure such as the pH level, the protein density and composition, $T_1\rho$ contrast has been applied in many pathological studies such as cerebral ischemia (Grohn et al., 2000; Kettunen et al., 2001), and neurodegenerative diseases (Borthakur et al., 2006; Michaeli et al., 2007).

Functional increases in $T_1\rho$ have been observed during visual stimulation in humans (Hulvershorn et al., 2005; Magnotta et al., 2012). Very recently, Magnotta et al. showed that activation-induced increase of $T_1\rho$ is better localized to tissue than conventional BOLD fMRI, suggesting that $T_1\rho$ is an attractive fMRI contrast. The source of $T_1\rho$ increase has been attributed to local tissue acidosis because $T_1\rho$ is sensitive to tissue pH via chemical exchange processes (Magnotta et al., 2012). However, earlier studies suggested that a local increase in cerebral blood volume (CBV) is the dominant factor of functional $T_1\rho$ increase (Hulvershorn et al., 2005) because blood $T_1\rho$ is much longer than tissue $T_1\rho$ (Hulvershorn et al., 2005; Kettunen et al., 2002; Magnotta et al., 2012). Since $T_1\rho$ is affected by the blood oxygenation (Hulvershorn et al., 2005; Kettunen et al., 2002), intravascular $T_1\rho$ change may also contribute. Additionally, other changes, such as a functional change in the cerebrospinal fluid (CSF) volume fraction (Jin and Kim, 2010), or a decrease in the concentration of metabolites, may also affect functional $T_1\rho$ signal. Since the utility of $T_1\rho$ fMRI is closely dependent on its signal origin, it is critical to untangle multiple potential sources.

This study aims to address two issues regarding $T_1\rho$ fMRI signal: 1) whether the signal originated from tissue, not blood can be detected, and 2) if detectable, what might be its possible source. The task-induced $T_1\rho$ response was evaluated in three steps. First, to separate the contributions of tissue versus blood and CSF to functional $T_1\rho$ response and to examine the detectability of tissue-originated $T_1\rho$ fMRI signal, high-resolution functional studies were performed on the cat visual cortex without and with suppression of the blood signal by using an intravascular contrast agent. Then, temporal and spatial properties of the $T_1\rho$ response were assessed. Second, to investigate potential sources of functional tissue $T_1\rho$ change, $T_1\rho$ experiments were performed in rats with the suppression of blood signals during hyperoxia, pH-decreasing hypercapnia and global ischemia, and susceptibility variations induced by i.v. injection of iron oxide. Third, to better understand possible source of *in vivo* $T_1\rho$ change, $T_1\rho$ was measured in protein and metabolite phantoms with different

pH and metabolite concentrations. Since $T_1\rho$ of tissue water measured with different SL frequencies are sensitive to molecular motion with different correlation times (Duvvuri et al., 2001; Makela et al., 2001), two or more ω_1 values were studied to shed light on the underlying mechanism. Throughout the whole text, we will use "tissue $T_1\rho$" to indicate $T_1\rho$ measured after the suppression of the blood signal. Preliminary findings were reported as meeting abstracts previously (Jin and Kim, 2009, 2011).

Materials and Methods

Theoretical basis of spin-lock fMRI

The pulse sequence for the SL experiment was a double spin-echo echo-planar imaging (EPI) sequence with a non-selective adiabatic SL preparation (Fig. 1A), where the amplitude and frequency modulation of the adiabatic SL preparation is illustrated in Fig. 1B. Namely, a 2-ms adiabatic half passage pulse was followed by a ramp of 0.5 ms, during which the amplitude of radiofrequency (RF) pulse was decreased to the desired SL field (B_1) and then held constant for the spin-locking time (TSL) (Grohn et al., 2005; Jin and Kim, 2010). Following the spin locking preparation, transverse spins were refocused using two adiabatic full-passage RF pulses with slice-selection gradients, therefore, $T_1\rho$-weighted images are additionally weighted by T_2 during the echo time (TE).

If a voxel contains multiple compartments such as blood, tissue and CSF, the TSL-dependent MR signal can be expressed as

$$S(TSL) = \sum_i V_i \cdot M_i \cdot \exp\left(-TSL/T_{1\rho,i}\right) \cdot \exp\left(-TE/T_{2,i}\right) \quad [1]$$

where i = arterial blood, venous blood, tissue water and CSF, and V and M are the volume fraction and the water proton magnetization of each compartment at TSL and TE = 0, respectively. In order to determine $T_1\rho$, $T_1\rho$-weighted images are generally acquired with multiple TSL values and then fitted by a mono-exponential function of TSL. The *apparent* $T_1\rho$ obtained will have contributions from all compartments, thus the data interpretation is complex. In particular, the *apparent* $T_1\rho$ may be modulated by a change of $T_1\rho$ value in any compartment or a change of any one of the weighting functions (e.g., V, M, or T_2).

When the blood signal is suppressed, the signal in parenchyma (without CSF) would reduce to a single compartment:

$$S(TSL) = V_{tissue} \cdot M_{tissue} \cdot \exp\left(-TSL/T_{1\rho,tissue}\right) \cdot \exp\left(-TE/T_{2,tissue}\right) \quad [2]$$

Hence, the tissue $T_1\rho$ can be extracted by multiple TSL measurements from high-resolution fMRI data without CSF. The functional change in total $T_1\rho$ obtained with Eq. [1] may surrogate the change in tissue $T_1\rho$ only if the contributions from other compartments are small and do not change significantly during activation.

$R_1\rho$ (=$1/T_1\rho$) equals $R_{2,0} + R_{ex}$ where R_{ex} is the chemical exchange-mediated relaxation rate, and $R_{2,0}$ is the transverse relaxation rate in the absence of chemical exchange. For a simple two-pool SL model with asymmetric population approximation (Jin et al., 2011; Trott and Palmer, 2002), R_{ex} can be described as

$$R_{ex} \approx \frac{p \cdot \delta^2 \cdot k}{\delta^2 + \omega_1^2 + k^2}, \quad [3]$$

or normalized as

$$\frac{R_{ex}}{p\delta} \approx \frac{k/\delta}{1+(\omega_1/\delta)^2+(k/\delta)^2}, \quad [4]$$

where p is the relative population of the labile proton which is assumed to be much smaller than water (i.e., $p << 1$), and k and δ are the exchange rate and the chemical shift between the labile proton and water, respectively. For a given ω_1/δ value, maximum R_{ex} occurs when $k/\delta = \sqrt{1+\omega_1^2/\delta^2}$. Thus, R_{ex} at very low ω_1 is optimized for intermediate exchanges ($k/\delta \sim 1$). To understand the contribution of different chemical exchange rates to $R_1\rho$, R_{ex} as a function of ω_1/δ was calculated from Eq. [4].

Animal preparation and stimulation

The animal protocol was approved by the Institutional Animal Care and Use Committee at the University of Pittsburgh. Female adolescent cats weighing 1.1 - 1.7 kg were used for visual stimulation studies, while Sprague-Dawley rats weighing 318 - 492 g were used for global modulation studies. Cats were treated with atropine sulfate (0.05 mg/kg, I.M.) and initially anesthetized with a cocktail of ketamine (10-25 mg/kg, I.M.) and xylazine (2.5 mg/kg, I.M.), while rats were initially anesthetized with 5% isoflurane. Then, both species were intubated and mechanically ventilated, and 2.0-2.2% isoflurane in a mixture of 70% N_2 and 30% oxygen was used during surgery. The femoral vein was cannulated to deliver maintenance fluid with pancuronium bromide (0.2 mg/kg per hour) and to inject contrast agent, and the femoral artery was catheterized to monitor the arterial blood pressure and to obtain blood samples for arterial blood gas measurements. During MRI experiments, the isoflurane level was maintained at 1.1 ± 0.2% isoflurane for cats and 1.5% for rats. End-tidal CO_2 level was kept within 3.5 ± 0.5% and the rectal temperature was controlled at 38.5 ± 0.5°C using a water circulating pad. The visual stimuli for cat functional studies were binocular, full-field, black and white, square-wave drifting gratings (spatial frequency 0.15 cycle/degree and temporal frequency 2 cycles/s). A gray screen was presented for the control. For gas challenge studies, a home-built electronic gas switching system was used to switch between two different gas mixtures.

MR experiments

All MRI experiments were performed on a 9.4 T MR system (Varian, Palo Alto, California, USA). For phantom experiments, a 3.8-cm diameter volume coil (Rapid Biomedical, Ohio) was used for both transmission and reception. For *in vivo* experiments, a custom-made single-loop surface coil with diameter of 1.6 cm was chosen to achieve high spatial resolution and high sensitivity, and also to reduce power deposition induced by a spin-locking pulse. A surface coil setup has been used in many $T_1\rho$ studies (Borthakur et al., 2004; Grohn et al., 2005; Hakumaki et al., 2002; Koskinen et al., 2006; Makela et al., 2004; Xu et al., 2008), where the adiabatic SL pulse is essential to nutate all spins within our region of interest (ROI) to the transverse plane. The adiabatic SL condition was determined from simulations of the Bloch Equations, and calibrated to ensure that such condition was achieved for most of the primary visual area. This is further confirmed by evaluating the quality of $T_1\rho$-weighted images (Fig. 1C vs. 1D), such that no ringing or stripe artifact was observed. The $T_1\rho$ measurement with the adiabatic SL sequence using a surface coil had been validated previously by phantom studies with a conventional SL sequence using a homogeneous coil (data not shown).

To evaluate the spatial heterogeneity of RF fields, the B_1 map was measured using a square pulse (to replace the SL preparation pulse in Fig. 1), where the pulse length was incremented such that signal intensity oscillated for several cycles in each imaging voxel, and the

nutation frequency of this oscillation (ω_1) was obtained (Jin and Kim, 2010). The spatial heterogeneity of B_1 within our ROIs was negligible for rat studies (see Fig. 5A inset below), but significant for cat experiments where the ROI were much larger. In a representative ω_1 map of cat brain (Fig. 1E), the ω_1 frequency was about 600 Hz at a region close to the coil (red square) and 400 Hz at a region distal from the coil (blue square). Nevertheless, the $R_1\rho$ maps showed very small spatial variance within the cat dorsal cortical area because the $R_1\rho$ dispersion is small in this low frequency range (Fig. 1F). To ensure similar ω_1 was applied to all animals, the middle cortical ROI (see below) was first determined from anatomical images, then the transmit power was adjusted so that the averaged ω_1 during TSL reached the targeted value, e.g., 500 or 2000 Hz. The averaged ω_1 and $R_1\rho$ values on each ROI were reported in texts.

***In vivo* experiments—**FLASH or T_1-weighted spin-echo EPI was used to obtain anatomic images with 128 × 128 matrix. Single slice was chosen for *in vivo* functional studies. In cats, multi-slice scout fMRI was used for the selection of the imaging slice. To suppress the intravascular signal, dextran-coated monocrystalline iron oxide nanoparticles (MION) were injected i.v. to greatly shorten blood T_2. Five sets of *in vivo* experiments were performed to measure $R_1\rho$ (= $1/T_1\rho$) changes: 1) $R_1\rho$ with and without blood contributions during cat visual stimulation, 2) tissue $R_1\rho$ (without blood contributions) at two ω_1 values during cat visual stimulation, 3) tissue $R_1\rho$ at four ω_1 values during two injections of MION, 4) tissue $R_1\rho$ at two ω_1 values during hypercapnia and hyperoxia, and 5) tissue $R_1\rho$ at multiple ω_1 values during global ischemia. Specifically, the experimental designs were:

Expt. I: $T_1\rho$ fMRI (n = 6 cats) was performed with ω_1 = 500 Hz on the visual cortex before and after the injection of 5 mg/kg of MION. The averaged SL frequency was ω_1 = 492 ± 26 Hz at a middle cortical ROI (see Fig. 2B below). After the $T_1\rho$ fMRI experiments in 5 out of the 6 animals, the CBV response was measured with injection of 10-13 mg/kg MION using double spin-echo EPI with TE of 40 ms to compare the temporal and spatial characteristics. Each fMRI run consisted of 40 s control, 40 s stimulation, and 60 s control; and there was ~1 minute resting time between each run. Twenty to forty runs were averaged for $T_1\rho$ fMRI experiments and ~10 runs averaged for CBV experiments.

Expt. II: To examine the effect of SL frequency ω_1, tissue $T_1\rho$ responses were measured after the injection of 5 mg/kg of MION during cat visual stimulation at two ω_1 values of 500 and 2000 Hz (n = 6 cats). The stimulation paradigm for cat visual stimulation was 20 s control, followed by 20 s stimulation and then 30 s control.

Expt. III: To confirm that tissue $R_1\rho$ measurement is insensitive to the intravascular susceptibility with ω_1 values applied in our studies, 2 mg/kg of MION were initially injected to suppress the blood signal. Then, dynamic changes of tissue R_2 and $R_1\rho$ with ω_1 of 125, 250, 500, and 2000 Hz (n = 4 rats) were measured during two separate injections of 1 mg/kg MION.

Expt. IV: Tissue $T_1\rho$ responses were measured after the injection of 5 mg/kg of MION during hyperoxic (60% O_2, n = 5 rats) and hypercapnic stimulations (8% CO_2, n = 5 rats) at ω_1 values of 500 and 2000 Hz. Hyperoxic and hypercapnic stimulations were achieved by inhalation of 60% of O_2 for 3 minutes and 8% CO_2 for 6 minutes, respectively. Hyperoxia challenge induces a drop in cerebral blood flow (CBF) and CBV (Lu et al., 2009), as well as an increase in the intravascular and extravascular oxygen level. On the other hand, hypercapnia challenge induces an increase of CBF and CBV, and a decrease in tissue pH.

Expt. V: Tissue $T_1\rho$ responses were measured after the injection of 1-5 mg/kg of MION during global ischemia induced by KCl injection, with ω_1 values of 250, 500, 1000, 2000 and 4000 Hz (n = 6 rats).

Although measurement of more TSL values would allow better accuracy for $T_1\rho$ quantification, it increases scan time and reduces the temporal resolution; therefore, only two TSL values were chosen for dynamic functional studies. In each fMRI experiment, TSL = 0 and TSL = 50 ms images for each ω_1 value were acquired in an interleaved manner. For experiments with multiple runs (Expt. I, II, and IV), the order of the images was alternated for different runs. Imaging data were acquired using a 2×2 cm^2 field of view and a 2 mm slice thickness for cat visual stimulation (Experiment I and II) and rat hypercapnic experiments (Experiment IV), and a 2.56×2.56 cm^2 field of view and a 4 mm slice thickness for rat hyperoxia (Experiment IV) and global ischemia experiments (Experiment V). The spin-echo time was TE = 25 ms, and the repetition time (TR) was 2.5 s for global ischemia and 2 s for all other experiments. Although 1-2 mg/kg of MION is already sufficient to suppress the blood signal (Kim and Kim, 2005), in fMRI experiments a higher dose of 5 mg/kg were chosen so that the BOLD effect would be roughly canceled by an increase in the MION susceptibility due to vessel dilation (Lu et al., 2007), minimizing any residue effect from susceptibility change to our tissue $R_1\rho$ measurement. The intravascular half-life for MION was measured to be 2.5 to 6 hour for cat while ~10 hours for rat. Thus, in all cat experiments with MION injection, the susceptibility effect was frequently monitored by measuring parenchyma T_2 values, and additional doses were injected when necessary to maintain a relatively stable MION level.

Phantom experiments—At SL frequencies usually applied for *in vivo* studies, $R_1\rho$ relaxation is highly sensitive to chemical exchange process between water and the labile non-water protons of protein and metabolites (Duvvuri et al., 2001; Jin et al., 2011; Makela et al., 2001). An acidosis-induced $T_1\rho$ increase has been suggested by Magnotta et al. as the dominant contributor to the functional signal, which was also illustrated in pH-varied protein phantoms and explained by a slowdown of chemical exchange between amide protons of protein backbone and water (Magnotta et al., 2012). It should be noted that $R_1\rho$ relaxation is not specific and has contributions from all relaxation pathways including chemical exchange processes from all labile protons. Besides proteins, $T_1\rho$ is also very sensitive to metabolites which may have different pH-dependence on SL frequencies. For example, we have shown that $T_1\rho$ is much more sensitive to labile protons with intermediate exchange rate, e.g., amines or hydroxyls groups, as compared to the slow exchanging amides (Jin et al., 2011). In particular, the amine-water proton exchanges from free metabolites are likely much faster than the overall chemical exchange rate of proteins (Zong et al., 2013).

Since chemical exchange contribution to $R_1\rho$ relaxation is dependent on pH, to further examine the possible sources of *in vivo* $R_1\rho$ change, three different pH phantoms were studied at 37°C:

#1.1. 8% of native bovine serum albumin (BSA) with four pH values of 6.0, 6.5, 7.0, and 7.5,

#1.2. 4% native egg-white albumin (EWA) with three pH values of 6.2, 6.8, and 7.4, and

#1.3. 4% EWA and 30 mM glutamate (Glu) with three pH of 6.2, 6.8, and 7.4.

All Phantoms above were dissolved in phosphate buffer saline (PBS) containing 10 mM of phosphate with 0.1 mM $MnCl_2$.

The purpose of Phantoms #1.1-#1.3 experiments is to qualitatively compare the pH-dependence of protein-only phantom versus protein phantom containing faster chemical exchanging metabolites. Because there are many amine-containing metabolites in brain, 30 mM Glu was chosen to roughly represent the total amine concentration from free metabolites.

The chemical exchange contributions to $R_1\rho$ from metabolites are mostly arisen from amine and hydroxyl protons. In order to separate the contributions of amine vs. hydroxyl proton exchanges to $R_1\rho$, two concentration-dependent phantom experiments were performed at 37°C as

#2.1. Glu with amine protons of 0, 10 and 20 mM in 2.2% agarose with 0.07 mM of $MnCl_2$ at pH = 7.0, and

#2.2. glucose (Glc) with hydroxyl protons of 0, 5, 10, 20 mM in PBS with 0.1 mM $MnCl_2$ at pH = 7.0.

The $R_1\rho$ dispersion properties of metabolites with hydroxyl versus amine protons will be compared to determine whether they can be differentiated by $R_1\rho$ measurements at 500 and 2000 Hz. The exchange-mediated relaxation rate R_{ex} is linearly proportional to the metabolite concentration (Jin et al., 2011). Thus, instead of measuring a small concentration of metabolites directly, where the accuracy may be limited because of the small R_{ex} compared to a much larger intrinsic $R_{2,0}$ in our phantoms with agarose or $MnCl_2$, we chose an alternative approach to obtain R_{ex} per mM of metabolite by fitting to data with three to four different concentrations.

In all phantoms, agarose and/or $MnCl_2$ was added to decrease the T_2 of water closer to *in vivo* values, but without changing the chemical exchange contributions to $R_1\rho$ (Jin and Kim, 2012). For each phantom, $R_1\rho$ values were measured for eleven ω_1 values of 125 Hz to 4000 Hz, by eleven TSL values (the range was varied for different phantoms, from 0 ms to approximately two T_2 values).

Data analysis

Data was analyzed with in-house Matlab® programs and STIMULATE software (Strupp, 1996). For functional experiments, images were first zero-filled to 128 × 128 and smoothed with a Gaussian filter with a full-width-half-maximum of 3 pixels. The EPI images were then compared with the anatomical image, if in-plane motions were more than 1 pixel, then those runs were excluded for signal averaging. Runs with same ω_1 and TSL values were grouped together and averaged. Then, *in vivo* $R_1\rho$ images for each time point were calculated from mono-exponential fitting of signal intensities on the two TSL-values (0 and 50 ms), as $R_1\rho = \ln(S_{TSL=0}/S_{TSL=50ms})/50ms$, and $\Delta R_1\rho$ was calculated from the difference between the $R_1\rho$ values averaged over the activation and baseline periods. In each experiment, T_2-weighted BOLD with TSL of 0 ms, $T_1\rho$-weighted fMRI with TSL of 50 ms, and $R_1\rho$ fMRI runs were obtained. For Expt. III, the ρR_2 time course was also calculated from the linear relationship between the relative signal change and TE as: $\Delta R_2 = -[(S - S_0)/S_0]/TE$ (Ogawa et al., 1993), where the baseline signal S_0 was defined as the averaged signal before the MION injection.

For fMRI, the Student's *t*-test was performed on a pixel-by-pixel basis to detect the activated area. First, a *p*-value threshold was chosen ($p < 0.01$ for experiment I - III, and $p < 0.05$ for experiment IV, uncorrected for multiple comparisons), and a minimal cluster size of eight pixels was applied. To calculate the CBV fMRI response, a correction of BOLD effect was performed (Zhao et al., 2006). Quantitative analyses were performed on the ROI determined from the anatomic images, regardless of whether these pixels pass the statistical threshold.

Two ROIs were chosen at the middle and surface of the visual cortex for cat studies, respectively, while one ROI was selected at the middle of the cortex for rat studies. To measure the rising times, the time courses of BOLD, CBV, and $R_1\rho$ before and after MION for each animal were interpolated to 200 ms temporal resolution, and the time from stimulus onset to 50% of the peak change was obtained, and paired Student's *t*-test was performed to evaluate the difference in rising time of the BOLD, CBV, and $R_1\rho$ responses. The averaged data were reported by mean and standard deviation (SD), and standard error of mean (SEM) for all time courses in the figures.

Results

Functional change of the $T_1\rho$ without and with suppression of blood signals

Since an imaging voxel contains blood, extravascular tissue and CSF with different $T_1\rho$ values, the change in the relative composition and/or the $T_1\rho$ of these compartments will modulate the measured $T_1\rho$ value (see Eq. [1]), and it has been reported in human visual stimulation and rat hypercapnia challenge studies that vessel dilation will lengthen $T_1\rho$ (Hulvershorn et al., 2005; Kettunen et al., 2002). Thus, it is critical to separate functional $T_1\rho$ changes originating from blood and tissue. To address this issue, we performed fMRI studies on six animals with and without suppression of blood signals by MION injection (Experiment I). A well-established layer model of the cat visual cortex was employed to examine whether functional $T_1\rho$ changes are localized to the most active sites, as suggested by Magnotta et al. (Magnotta et al., 2012). The middle cortical layer (layer IV) is known to have the highest change in neuronal activities and in metabolic rate during stimulation (Price, 1983; Tieman and Tumosa, 1983) and can be visualized as a slightly bright band (indicated by arrows) in the cat visual cortex (outlined by green contours) in T_1-weighted inversion recovery echo-planar images (Fig. 2A) (Jin and Kim, 2008c; Kim and Kim, 2011).

The T_2-weighted fMRI map before MION injection shows significant stimulation-induced signal increase in gray matter (outlined in green) within the visual cortex (Fig. 2C) as expected from BOLD contrast (Zhao et al., 2006). When $T_1\rho$-weighting with ω_1 of 500 Hz was applied (Fig. 2D), a higher percentage signal change was detected within the parenchyma. Functional $R_1\rho$ maps calculated from T_2-weighted and $T_1\rho$-weighted fMRI show a decrease in $R_1\rho$ (*i.e.*, increase in $T_1\rho$) in the parenchyma for without (Fig. 2E) and with blood suppression (Fig. 2F), indicating that extravascular tissue $R_1\rho$ change indeed exists. Note that negative fMRI signal changes (blue/purple pixels in Fig. 2C and 2D) and $R_1\rho$ increases (red/yellow pixels in Fig. 2E and 2F) were observed at the boundary of the cortical surface and CSF. This is most likely due to a reduction of CSF partial volume caused by functional vessel dilation (Jin and Kim, 2010; Piechnik et al., 2009; Scouten and Constable, 2008) because R_2 and $R_1\rho$ values of CSF are much smaller than those of tissue water (*e.g.*, $R_1\rho$ of about 2.2 s^{-1} vs. 21 s^{-1} at 9.4 T (Jin and Kim, 2010)).

Fig. 2G compared the functional ΔR_2 and $\Delta R_1\rho$ from an ROI drawn at the middle cortical layer disregarding the statistical thresholds for activation (Fig. 2B). Large difference in the functional ΔR_2 before and after MION (-0.343 ± 0.029 s^{-1} vs. -0.022 ± 0.031 s^{-1}) were observed, because for the latter case the BOLD effect was nearly canceled by the vessel dilation-induced increase of MION concentration (Lu et al., 2007). In contrast ~63% of the functional $\Delta R_1\rho$ remains after the blood signal is suppressed (0.081 ± 0.013 s^{-1} vs. 0.051 ± 0.008 s^{-1}), indicating that even though intravascular signals contribute to functional $\Delta R_1\rho$, tissue $R_1\rho$ fMRI signals dominate during visual stimulation at 9.4 T.

Temporal properties of $T_1\rho$ fMRI signal at the middle cortical layer

Characteristics of dynamic functional changes can provide insights into the source of $R_1\rho$ fMRI. The averaged time courses (n = 6 animals) of the fMRI response at the middle cortical ROI (see Fig. 2B) were shown for both conditions without (Fig. 3A) and with MION (Fig. 3B). In both cases the runs with TSL = 50 ms and ω_1 of 500 Hz (red) have larger positive signal changes than those with TSL = 0 (blue), whereas the post-stimulus undershoots are similar. To compare with $R_1\rho$ and BOLD fMRI time courses, CBV fMRI studies were also performed in five animals after an intravascular MION injection of 10-13 mg/kg. During the 40-s stimulation period, $R_1\rho$ without MION, BOLD and CBV responses decreased gradually following its peak (Fig. 3D), while tissue $R_1\rho$ with MION almost remained on a plateau (Fig. 3C). After the stimulus offset, the post-stimulus undershoot was prominent in BOLD and CBV (Fig. 3D), but not in tissue $R_1\rho$ with MION (Fig. 3C). To further evaluate their temporal behavior, the normalized time courses were compared for the SE-BOLD, CBV, and $R_1\rho$ before and after MION (Fig. 3E). The time to 50% of the peak occurs in the order of tissue $R_1\rho$, $R_1\rho$ (without MION), BOLD, and CBV (dotted line). The rising time of tissue $R_1\rho$ is 1.1 s and 1.7 s faster than the BOLD (n = 5, $p < 0.05$) and CBV ($p < 0.01$) responses, respectively (Fig. 3F). These temporal characteristics suggest that the tissue $R_1\rho$ change induced by stimulation has origins different from hemodynamics as in BOLD and CBV fMRI.

SL frequency dependence of tissue $R_1\rho$ changes during visual stimulation

Since $T_1\rho$ is sensitive to molecular motions with correlation time τ close to $1/2\pi\omega_1$, SL frequency dependency studies may provide insights into functional $R_1\rho$ changes. Thus, $T_1\rho$ fMRI studies were performed with ω_1 of 500 and 2000 Hz after the suppression of blood signals with MION during 40-s visual stimulation (n = 6 cats; Expt. II). The baseline $R_1\rho$ values at the middle cortical ROI were 21.0 ± 0.14 s^{-1} and 17.55 ± 0.13 s^{-1} for ω_1 = 500 and 2000 Hz, respectively, similar to previous values measured at the rat cortex (Makela et al., 2004). At ω_1 = 500 Hz, the temporal variation of $R_1\rho$ in the baseline period is 0.012 ± 0.002 s^{-1} (n = 6). When ω_1 increases from 500 Hz to 2000 Hz for visual stimulation studies, the increase of $R_1\rho$ remains similar at the boundary of the cortical surface and CSF, while the decrease of $R_1\rho$ at the middle of the cortex almost disappears (Fig. 4A and 4C for 500 Hz vs. 4B and 4D for 2000 Hz). Since the $R_1\rho$ change at the cortical surface is dominated by changes to the CSF volume fraction, it is to be expected that it is insensitive to SL frequencies. However, the functional $R_1\rho$ *decrease* at the middle cortical ROI for 500 Hz is 0.049 s^{-1} and 2.7 times larger ($p < 0.005$) than at 2000 Hz (Fig. 4E). This experiment indicates tissue $R_1\rho$ change is highly dependent on SL frequency, suggesting its source is from the slow molecular motion of tissue water rather than vascular response.

Tissue $T_1\rho$ is insensitive to intravascular susceptibility changes

Functional $R_1\rho$ change may be influenced by blood susceptibility effects due to insufficient spin locking. To achieve effective spin locking, the B_1 field should be much higher than the local magnetic field inhomogeneity. If B_1 is close to 0, the transverse spins are not locked and would relax by diffusion across the inhomogeneous field; therefore, $T_1\rho$ approaches T_2. With high spin-locking frequency (ω_1 = 2500 Hz), it has been reported that the $T_1\rho$ of extravascular water is almost unaffected by intravascular susceptibility effects (Kettunen et al., 2002), such as from a variation of paramagnetic deoxyhemoglobin, *i.e.,* the BOLD effect. However, this may not be true for lower ω_1 values usually applied for *in vivo* studies due to the limitation of RF power deposition. To assess whether a change of intravascular susceptibility may affect $T_1\rho$ of tissue water for our imaging parameters, $T_1\rho$ was measured in the rat cortex under two intravascular injections of 1 mg Fe/kg MION (Expt. III, n = 4 rats). Before each experiment, 2 mg Fe/kg MION was injected i.v. to fully suppressed the intravascular signal. In the extravascular tissue, the susceptibility change induced a large

modulation in R_2 but much smaller change in $R_1\rho$ with ω_1 = 125 Hz (Fig. 5A), and the change in $R_1\rho$ is minimal for $\omega_1 \geq 500$ Hz, indicating that tissue $R_1\rho$ is insensitive to changes in blood susceptibility for SL frequencies applied in our functional $T_1\rho$ experiments.

Tissue $T_1\rho$ is insensitive to hyperoxia-induced hemodynamic changes

In addition to a change of vascular susceptibility, hemodynamics also induces small change in tissue microstructure/microenvironment such as a modulation of the extracellular oxygenation level, perfusion, and local cellular structural distortion caused by vessel volume change. Whether these vascular-originated effects will alter extravascular $T_1\rho$ is examined by a hyperoxia challenge with the suppression of blood (Exp. IV, n = 5 rats). During inhalation of 60% O_2, a large decrease of tissue R_2 (i.e., an increase in BOLD signal) was observed due to reduction of intravascular susceptibility (Fig. 5B). In contrast, the change in tissue $R_1\rho$ change is minimal for both ω_1 of 500 and 2000 Hz. This experiment suggested that in addition to intravascular susceptibility, the tissue $R_1\rho$ should also be insensitive to modulations of extracellular oxygenation level, perfusion, and local cellular structural distortion caused by vessel volume change.

Tissue $R_1\rho$ changes during hypercapnic challenge and global ischemia

Tissue $R_1\rho$ decreases (i.e., $T_1\rho$ increases) may be caused by a change of chemical exchange between water and exchangeable protons resulting from a suggested drop in pH during stimulation; a similar change was observed during pH-decreasing hypercapnic challenge at 3 T (Magnotta et al., 2012). However, similar hemodynamic changes, i.e., increase of CBV and CBF, occur for both cases, potentially leading to similar $R_1\rho$ changes if the intravascular contribution is significant (Hulvershorn et al., 2005). Thus, it is important to compare tissue $R_1\rho$ changes induced by visual stimulation and hypercapnic challenge, after the suppression of intravascular contribution. Unlike the observation during visual stimulation in our studies (Figs. 2 – 4), during hypercapnic challenge the tissue $R_1\rho$ *increases* (i.e., $T_1\rho$ decreases) at the rat cortex for ω_1 of 500 Hz, but slightly *decreases* for ω_1 of 2000 Hz at 9.4 T (Fig. 6A). The averaged time course of $R_1\rho$ obtained from the middle cortical ROI shows a large positive change for ω_1 = 500 Hz, but a small negative change for 2000 Hz (Fig. 6B).

While an ω_1-dependence of $R_1\rho$ was expected and had been reported in previous ischemia studies at 4.7 T (Grohn et al., 2000; Kettunen et al., 2002), the observation of opposite polarity of $R_1\rho$ change for the two ω_1 values of 500 and 2000 Hz is surprising. To examine whether this is a distinct property for tissue pH decrease at our high field of 9.4 T, we measured the tissue $R_1\rho$ response for more ω_1 values during the initial period of rat global ischemia induced by potassium chloride injection which is well-known to cause tissue acidosis (n = 6 animals; Experiment V) (Kettunen et al., 2002). Tissue $R_1\rho$ increases rapidly after KCl injection for $\omega_1 \leq 1000$ Hz and decreases for $\omega_1 \geq 2000$ Hz, similar to the results for hypercapnic challenge, albeit of much larger magnitudes. The change in tissue $R_1\rho$ reached a maximum at ~ 3 minutes post-KCl then showed a similar rate of decrease for all the ω_1 values in following 15 minutes or so. These observations are quite different from visual stimulation studies, in particular, tissue $R_1\rho$ change with ω_1 = 500 Hz is negative for visual stimulation (Fig. 3C), but positive for tissue acidosis (global ischemia and hypercapnia) (Fig. 6B-C), indicating that neural stimulation-induced tissue $R_1\rho$ decrease is not due to tissue acidosis.

$T_1\rho$ measurements of protein and metabolite phantoms

To gain more insight into the difference of tissue $R_1\rho$ changes during tissue acidosis and neural stimulation, ω_1-dependent phantom experiments were performed and compared to theoretical models. Using Eq. [4], $R_{ex}/(p\delta)$ was plotted against ω_1/δ at different exchange

rates (k/δ) (Fig. 7A). Note that an increase in R_{ex} leads to an increase in $R_1\rho$. In the case of tissue acidosis (i.e., a decrease of k/δ), if k/δ decreases from intermediate exchange to slow exchange ($k/\delta << 1$), R_{ex} would decrease for all ω_1 values (Fig. 7A, e.g., dashed green downward arrow). On contrary, if k/δ decreases from fast exchange ($k/\delta >> 1$) to intermediate exchange, the R_{ex} measured at a small ω_1 would increase (solid green upward arrow), and R_{ex} measured at a large ω_1 would decrease (solid orange downward arrow), exhibiting an opposite polarity of $R_1\rho$ change.

The $R_1\rho$ dispersions of BSA and EWA decrease similarly with pH in the ω_1 range of 125 to 4000 Hz (Fig. 7B and 7C). While proteins have many different labile protons with different exchange rates, these pH-dependence results suggest that the overall proton exchange of these proteins can be considered as in the slow to intermediate exchange regime at 9.4 T. The addition of Glu to EWA enhances $R_1\rho$ dispersion significantly and also changes its pH-dependence (Fig. 7C), suggesting that the amine-water proton exchange from Glu are much faster than those from proteins and falls into the intermediate to fast exchange category. When pH is decreased from 7.4 to 6.8, $R_1\rho$ increases for $\omega_1 \leq 1414$ Hz whereas $R_1\rho$ decreases for $\omega_1 \geq 2000$ Hz. This pH-dependent $R_1\rho$ change at 500 vs. 2000 Hz is qualitatively similar to hypercapnia (Fig. 6B) and early ischemia results (Fig. 6C), but is different from the neural stimulation-induced $R_1\rho$ changes (Fig. 4E).

Since $R_1\rho$ is also sensitive to the concentration of labile protons (Eq. [3]), the small decrease of $R_1\rho$ observed for neural stimulation might be caused by a reduction in the concentration of metabolites. In Fig. 8A and 8B, the $R_1\rho$ of both amine-containing Glu and hydroxyl-containing Glc phantoms increases linearly with concentration and decreases with ω_1, but their relative sensitivity at 500 vs. 2000 Hz is different due to the different chemical shifts and exchange rates of amine and hydroxyl protons (Jin et al., 2011; Liepinsh and Otting, 1996; van Zijl and Yadav, 2011). Although the concentrations of these metabolites are quite different from *in vivo* conditions, possible contributions from amine- or hydroxyl containing metabolite can be roughly estimated from 1) the linear-dependence of R_{ex} (and hence $R_1\rho$) on metabolite concentration (Eq. [3]), and 2) the difference of $R_1\rho$ for the two ω_1 values (500 and 2000 Hz) which is correlated with the exchange rate. The slope of $R_1\rho$ vs. Glu and Glc concentration is 0.11 and 0.067 $s^{-1} \cdot mM^{-1}$ for ω_1 of 500 Hz and 0.088 and 0.024 $s^{-1} \cdot mM^{-1}$ for ω_1 of 2000 Hz, respectively (Fig. 8C). The high sensitivity of $R_1\rho$ on metabolites indicates that the observed tissue $R_1\rho$ change of 0.051 s^{-1} at 500 Hz during visual stimulation could be explained by only sub-millimolar decrease of these metabolites. The ratio of slopes at ω_1 of 500 Hz to 2000 Hz is only 1.25 for Glu, but 2.8 for Glc which is very similar to the ratio of 2.7 observed in the visual stimulation studies. These results suggest that sub-millimolar decreases in metabolite concentrations, especially hydroxyl-containing metabolites such as glucose, potentially give rise to a plausible source of functional $R_1\rho$ decrease.

Discussions

Our results show that the source of activation-induced $T_1\rho$ change is complex and has both vascular and tissue originated components. The vascular-originated component is mostly due to a local volume redistribution effect in an imaging voxel, because there is a large difference between the $T_1\rho$ values of blood, tissue and CSF water. Specifically, vessel dilation would lengthen the *apparent* $T_1\rho$ in the parenchyma but would shorten it at the boundary of cortex and CSF. After the suppression of vascular signal, the observed tissue $T_1\rho$ signal in parenchyma is likely caused by an activation-induced change of tissue metabolism, based on following reasons. Tissue $T_1\rho$ response shows (i) a better localization to the middle cortical layer than BOLD response, is (ii) sensitive to the SL frequency, is (iii) faster than both BOLD and CBV, and has (iv) no post-stimulus undershoot unlike BOLD

and CBV. Its non-hemodynamic origin is also supported by the observation that tissue $R_1\rho$ is unaffected by tissue oxygenation, CBF and CBV changes induced by hyperoxia shown in Fig. 5B (Lu et al., 2009). Even though there have been intense efforts to develop non-hemodynamic tissue-specific fMRI methods for the last two decades (Bandettini et al., 2005; Chu et al., 2004; Jin and Kim, 2008b; Le Bihan et al., 2006; Miller et al., 2007; Parkes et al., 2007; Tang et al., 2008; Xiong et al., 2003), our results showed for the first time that with complete suppression of blood, a tissue-originated fMRI signal, while the sensitivity is much weaker than BOLD (Fig. 2G), can be consistently detected in brain *in vivo* using spin-lock fMRI.

$T_1\rho$ relaxation is highly dependent on experimental condition and experimental parameters such as B_0. Since the difference in $T_1\rho$ between the blood, tissue and CSF is dependent on magnetic field strength (B_0), the vascular contribution to functional change of $T_1\rho$ would also be B_0-dependent. Similarly, a functional change in tissue $T_1\rho$, if it is mainly caused by the proton-exchange effect, would also be B_0-dependent because a high field increases the chemical shifts between labile protons and water, and consequently the exchange-mediated relaxation rate (R_{ex} increases with δ in Eq. [3]). Thus, we postulate a larger tissue-originated $T_1\rho$ signal in the parenchyma at a higher B_0. Our results at 9.4 T showed that the *vascular contribution* to activation-induced $T_1\rho$ change is about 37% with ω_1 = 500 Hz at the brain parenchyma. At 3 T, an increase in end-tidal CO_2 (e.g., hypercapnia) decreases tissue pH and increases $T_1\rho$ value measured with ω_1 of 400 Hz, and it was recently suggested by Magnotta et al. that *in vivo* $T_1\rho$ increase during human visual stimulation is also due to tissue acidosis (Magnotta et al., 2012). While a correlation between tissue acidosis and $T_1\rho$ increase was established for hypercapnia, there was no evidence that the increase of $T_1\rho$ is mostly from the tissue compartment. Importantly, both visual stimulation and hypercapnia increase CBV, which will consequently lengthen the measured $T_1\rho$ due to longer $T_1\rho$ of blood relative to tissue. Indeed, the vascular contribution with ω_1 = 500 Hz was estimated to be dominant (> 90%) in a human $T_1\rho$ fMRI study at 3 T according to the estimation of Hulvershorn et al. (Hulvershorn et al., 2005). In our case with suppression of blood signal, tissue $T_1\rho$ at 500 Hz increases during visual stimulation but decreases for tissue acidosis, disagree with the interpretation of functional $T_1\rho$ change by Magnotta et al. (Magnotta et al., 2012).

$T_1\rho$ relaxation is also highly dependent on ω_1, and $T_1\rho$ dispersion studies with more than one ω_1 value would be necessary to shed light on the underlying mechanisms. During rat global ischemia at 4.7 T, Kettunen et al. reported an increase of $T_1\rho$ at $\omega_1 \geq 2500$ Hz, but marginal $T_1\rho$ change for ω_1 of ~850 Hz (Kettunen et al., 2001). In our experiments with suppression of blood signals at 9.4 T, $T_1\rho$ values during hypercapnia and the initial period of global ischemia decrease for $\omega_1 \leq 1000$ Hz, while increase for $\omega_1 \geq 2000$ Hz. This opposite polarity of $T_1\rho$ changes for low and high ω_1, especially the increase of $R_1\rho$ at a small ω_1 with decreasing pH, can be qualitatively explained by a proton-exchange mechanism where k is much faster than δ of contributing exchangeable protons relative to water at normal physiological pH, and becomes closer to δ during tissue acidosis (e.g., k/δ decreases from 3 to 1 in Fig. 7A). From phantom experiments (Fig. 7C), contributing protons with fast to intermediate exchanges can be mainly from metabolites, such as free amino acids. In our recent rat focal brain ischemia study (Zong et al., 2013), we have investigated the properties of amine-water proton exchange using off-resonance SL technique measured at a frequency offset 2.5 ppm from water. An increase in the off-resonance $R_1\rho$ with ω_1 of 500 Hz was observed due to slowdown of chemical exchanges during stroke, and the change of $R_1\rho$ is strongly correlated with pH and the concentration of glutamate and γ-aminobutyric acid (GABA). These findings are in good agreement with the on-resonance $R_1\rho$ results observed in current pH-dependent studies (Fig. 7C).

While a small local tissue acidosis might occur during visual stimulation (Lin et al., 2012; Magnotta et al., 2012), the difference in tissue $T_1\rho$ responses during visual stimulation versus hypercapnic challenge and global ischemia indicated that tissue acidosis is unlikely the major contributor to the neuronal activation-induced $T_1\rho$ signal. One plausible mechanism may be a local drop in metabolites concentration due to elevated consumption. For example, a decreased glucose concentration ranging from 0.13 to 0.51 $\mu mol \cdot g^{-1}$ has been reported in human magnetic resonance spectroscopy (MRS) studies during sustained visual stimulation of several minutes or more (Chen et al., 1993; Frahm et al., 1996; Lin et al., 2012; Mangia et al., 2007). The averaged change in $T_1\rho$ during our cat visual stimulation studies would correspond to a reduction in glucose concentration of ~0.6 $\mu mol \cdot g^{-1}$ (considering 0.83 g water/g tissue) for the middle cortical ROI, and ~0.3 $\mu mol \cdot g^{-1}$ for a larger ROI including part of white matter area (not shown). This concentration decrease estimated from functional $T_1\rho$ change falls well into the range of MRS results whose voxel should also have significant partial volume effect. Besides chemical exchange, there may be other contributions to the $T_1\rho$ fMRI signal. For example, the tissue component itself might also be sub-compartmentalized into different $T_1\rho$ pools, hence, a relative volume change between sub-compartments or variation in the rate of exchange in these sub-compartments, which has been suggested for the $T_1\rho$ contrast during ischemia (Jokivarsi et al., 2009), may occur as a results of neuronal cell-swelling and alter the observed $T_1\rho$. Further investigations are needed to determine the exact source of tissue-originated signals.

Conclusion

Functional $T_1\rho$ responses can be contributed by changes in blood, CSF and/or tissue signals. In order to detect tissue-originated functional responses, it is critical to remove the CSF contamination, and also to separate contributions of blood and tissue signals. While $T_1\rho$ fMRI with blood contribution has already been shown in human studies to offer better tissue-localization than the BOLD response with large contributions from draining veins (Hulvershorn et al., 2005; Magnotta et al., 2012), its utility may not be better than CBF and CBV-based fMRI which are also more specific to neural active sites than BOLD fMRI (Jin and Kim, 2008a; Zhao et al., 2006). In addition to the difficulty of fully removing the intravascular signal as well as the CSF contamination, the application of *tissue* $T_1\rho$ to human studies may be challenging due to the limitation on specific adsorption rate which increases quadratically with magnetic field strength, and also due to the reduced sensitivity compared to BOLD. On the other hand, functional tissue $T_1\rho$ change, albeit the sensitivity is still much lower than BOLD, can be consistently observed at 9.4 T. Tissue-originated $T_1\rho$ signal is faster than hemodynamic responses, has no post-stimulus undershoot unlike BOLD and CBV fMRI, and shows high specificity to middle cortical areas. Therefore, tissue $T_1\rho$ fMRI may potentially be exploited as a non-hemodynamic imaging tool for animal research.

Acknowledgments

We thank Ping Wang for animal preparation, Kristy Hendrich for maintaining the 9.4 T system, Dr. Risto Kauppinen and Joonas Autio for helpful discussions, and Hunter Mehrens for proof reading. This work is supported by NIH grants EB003324, EB003375, and NS44589.

References

Bandettini PA, Petridou N, Bodurka J. Direct detection of neuronal activity with MRI: Fantasy, possibility, or reality? Applied Magnetic Resonance. 2005; 29:65–88.

Borthakur A, Charagundla SR, Wheaton A, Reddy R. T-1ho-weighted MRI using a surface coil to transmit spin-lock pulses. Journal of Magnetic Resonance. 2004; 167:306–316. [PubMed: 15040987]

Borthakur A, Gur T, Wheaton AJ, Corbo M, Trojanowski JQ, Lee VMY, Reddy R. In vivo measurement of plaque burden in a mouse model of Alzheimer's disease. Journal of Magnetic Resonance Imaging. 2006; 24:1011–1017. [PubMed: 17036339]

Chen W, Novotny E, Zhu X-H, Rothman D, Shulman RG. Localized 1H NMR measurement of glucose consumption in human brain during visual stimulation. Proc Natl Acad Sci USA. 1993; 90:9896–9900. [PubMed: 8234332]

Chu RN, de Zwart JA, van Gelderen P, Fukunaga M, Kellman P, Holroyd T, Duyn JH. Hunting for neuronal currents: absence of rapid MRI signal changes during visual-evoked response. Neuroimage. 2004; 23:1059–1067. [PubMed: 15528106]

Duvvuri U, Goldberg AD, Kranz JK, Hoang L, Reddy R, Wehrli FW, Wand AJ, Englander SW, Leigh JS. Water magnetic relaxation dispersion in biological systems: The contribution of proton exchange and implications for the noninvasive detection of cartilage degradation. Proceedings of the National Academy of Sciences of the United States of America. 2001; 98:12479–12484. [PubMed: 11606754]

Editorial. Connecting the dots. Nature Neuroscience. 2009; 12:99–99.

Frahm J, Kruger KD, Merboldt KD, Kleinschmidt A. Dynamic uncoupling and recoupling of perfusion and oxidative metabolism during focal brain activation in man. Magn Reson Med. 1996; 35:143–148. [PubMed: 8622575]

Grohn HI, Michaeli S, Garwood M, Kauppinen RA, Grohn OHJ. Quantitative T-1rho and adiabatic Carr-Purcell T-2 magnetic resonance imaging of human occipital lobe at 4 T. Magnetic Resonance in Medicine. 2005; 54:14–19. [PubMed: 15968651]

Grohn OHJ, Kettunen MI, Makela HI, Penttonen M, Pitkanen A, Lukkarinen JA, Kauppinen RA. Early detection of irreversible cerebral ischemia in the rat using dispersion of the magnetic resonance imaging relaxation time, T1rho. Journal of Cerebral Blood Flow and Metabolism. 2000; 20:1457–1466. [PubMed: 11043908]

Hakumaki JM, Grohn OHJ, Tyynela K, Valonen P, Yla-Herttuala S, Kauppinen RA. Early gene therapy-induced apoptotic response in BT4C gliomas by magnetic resonance relaxation contrast T-1 in the rotating frame. Cancer Gene Therapy. 2002; 9:338–345. [PubMed: 11960284]

Hulvershorn J, Borthakur A, Bloy L, Gualtieri EE, Reddy R, Leigh JS, Elliott MA. T-1 rho contrast in functional magnetic resonance imaging. Magnetic Resonance in Medicine. 2005; 54:1155–1162. [PubMed: 16217783]

Jin T, Autio J, Obata T, Kim SG. Spin-locking versus chemical exchange saturation transfer MRI for investigating chemical exchange process between water and labile metabolite protons. Magnetic Resonance in Medicine. 2011; 65:1448–1460. [PubMed: 21500270]

Jin T, Kim S-G. Change of the cerebrospinal fluid volume during brain activation investigated by T1ρ-weighted fMRI. Neuroimag. 2010; 51:1378–1383.

Jin T, Kim SG. Cortical layer-dependent dynamic blood oxygenation, cerebral blood flow and cerebral blood volume responses during visual stimulation. Neuroimage. 2008a; 43:1–9. [PubMed: 18655837]

Jin T, Kim SG. Functional changes of apparent diffusion coefficient during visual stimulation investigated by diffusion-weighted gradient-echo fMRI. Neuroimage. 2008b; 41:801–812. [PubMed: 18450483]

Jin T, Kim SG. Improved cortical-layer specificity of vascular space occupancy fMRI with slab inversion relative to spin-echo BOLD at 9.4 T. Neuroimage. 2008c; 40:59–67. [PubMed: 18249010]

Jin, T.; Kim, SG. Separation of the vascular and tissue contributions to the T1rho change induced by brain activation.. Proc 19th ISMRM Annual Meeting. Proc 19th ISMRM Annual Meeting; Honolulu, Hawaii. 2009.

Jin, T.; Kim, SG. Dynamic changes in the tissue microenvironment induced by hypercapnia and hyperoxia: a T1rho dispersion study at 9.4 T.. Proc 19th ISMRM Annual Meeting. Proc 19th ISMRM Annual Meeting; Montreal, Canada. 2011.

Jin T, Kim SG. Quantitative Chemical Exchange Sensitive MRI Using Irradiation with Toggling Inversion Preparation. Magn Reson Med. 2012; 68:1056–1064. [PubMed: 22887701]

Jokivarsi KT, Niskanen JP, Michaeli S, Grohn H, Garwood M, Kauppinen RA, Grohn OH. Quantitative assessment of water pools by T 1 rho and T 2 rho MRI in acute cerebral ischemia of the rat. J Cereb Blood Flow Metab. 2009; 29:206–216. [PubMed: 18827834]

Kettunen MI, Grohn OHJ, Penttonen M, Kauppinen RA. Cerebral T-1 rho relaxation time increases immediately upon global ischemia in the rat independently of blood glucose and anoxic depolarization. Magnetic Resonance in Medicine. 2001; 46:565–572. [PubMed: 11550250]

Kettunen MI, Grohn OHJ, Silvennoinen MJ, Penttonen M, Kauppinen RA. Effects of intracellular pH, blood, and tissue oxygen tension on T-1 rho relaxation in rat brain. Magnetic Resonance in Medicine. 2002; 48:470–477. [PubMed: 12210911]

Kim SG, Ogawa S. Biophysical and physiological origins of blood oxygenation level-dependent fMRI signals. J Cereb Blood Flow and Metab. 2012; 32:1188–1206. [PubMed: 22395207]

Kim T, Kim SG. Quantification of Cerebral Arterial Blood Volume and Cerebral Blood Flow Using MRI With Modulation of Tissue and Vessel (MOTIVE) Signals. Magnetic Resonance in Medicine. 2005; 54:333–342. [PubMed: 16032688]

Kim T, Kim SG. Temporal dynamics and spatial specificity of arterial and venous blood volume changes during visual stimulation: implication for BOLD quantification. J Cereb Blood Flow and Metab. 2011; 31:1211–1222. [PubMed: 21179068]

Koskinen SK, Niemi PT, Kajander SA, Komu MES. T-1 rho Dispersion profile of rat tissues in vitro at very low locking fields. Magnetic Resonance Imaging. 2006; 24:295–299. [PubMed: 16563959]

Le Bihan D, Breton E, Lallemand D, Grenier P, Cabanis E, Laval-Jeantet M. MR imaging of intravoxel incoherent motions: application to diffusion and perfusion in neurologic disorders. Radiology. 1986; 161:401–407. [PubMed: 3763909]

Le Bihan D, Urayama S, Aso T, Hanakawa T, Fukuyama H. Direct and fast detection of neuronal activation in the human brain with diffusion MRI. Proceedings of the National Academy of Sciences of the United States of America. 2006; 103:8263–8268. [PubMed: 16702549]

Liepinsh E, Otting G. Proton exchange rates from amino acid side chains - Implications for image contrast. Magnetic Resonance in Medicine. 1996; 35:30–42. [PubMed: 8771020]

Lin Y, Stephenson MC, Xin L, Napolitano A, Morris PG. Investigating the metabolic changes due to visual stimulation using functional proton magnetic resonance spectroscopy at 7 T. J Cereb Blood Flow Metab. 2012; 32:1484–1495. [PubMed: 22434070]

Lu HB, Scholl CA, Zuo YT, Stein EA, Yang YH. Quantifying the Blood Oxygenation Level Dependent Effect in Cerebral Blood Volume–Weighted Functional MRI at 9.4T. Magn Reson Med. 2007; 58:616–621. [PubMed: 17763339]

Lu J, Dai GP, Egi Y, Huang S, Kwon SJ, Lo EH, Kim YR. Characterization of cerebrovascular responses to hyperoxia and hypercapnia using MRI in rat. Neuroimag. 2009; 45:1126–1134.

Magnotta VA, Heo H-Y, Dlouhy BJ, Dahdaleh NS, Follmer RL, Thedens DR, Welsh MJ, Wemmie JA. Detecting activity-evoked pH changes in human brain. Proc Nat Acad Sci. 2012; 109:8270–8273. [PubMed: 22566645]

Makela HI, De Vita E, Grohn OHJ, Kettunen MI, Kavec M, Lythgoe M, Garwood M, Ordidge R, Kauppinen RA. B-0 dependence of the on-resonance longitudinal relaxation time in the rotating frame (T-1p) in protein phantoms and rat brain in vivo. Magnetic Resonance in Medicine. 2004; 51:4–8. [PubMed: 14705038]

Makela HI, Grohn OHJ, Kettunen MI, Kauppinen RA. Proton exchange as a relaxation mechanism for T-1 in the rotating frame in native and immobilized protein solutions. Biochemical and Biophysical Research Communications. 2001; 289:813–818. [PubMed: 11735118]

Mangia S, Tkac I, Gruetter R, Van de Moortele PF, Maraviglia B, Ugurbil K. Sustained neuronal activation raises oxidative metabolism to a new steady-state level: evidence from H-1 NMR spectroscopy in the human visual cortex. Journal of Cerebral Blood Flow and Metabolism. 2007; 27:1055–1063. [PubMed: 17033694]

Michaeli S, Oz G, Sorce DJ, Garwood M, Ugurbil K, Majestic S, Tuite P. Assessment of brain iron and neuronal integrity in patients with Parkinson's disease using novel MRI contrasts. Movement Disorders. 2007; 22:334–340. [PubMed: 17149719]

Miller KL, Bulte DP, Delvlin H, Robson MD, Wise RG, Woolrich MW, Jezzard P, Behrens TE. Evidence for a vascular contribution to diffusion fMRI at high b value. Proc Nat Acad Sci. 2007; 104:20967–20973. [PubMed: 18093924]

Ogawa S, Menon RS, Tank DW, Kim S-G, Merkle H, Ellermann JM, Ugurbil K. Functional Brain Mapping by Blood Oxygenation Level-Dependent Contrast Magnetic Resonance Imaging. Biophys J. 1993; 64:800–812.

Park TS, Lee SY, Park JH. Effect of nerve cell currents on MRI images in snail ganglia. Neuroreport. 2004; 15:2783–2786. [PubMed: 15597054]

Parkes LM, de Lange FP, Fries P, Toni I, Norris DG. Inability to directly detect magnetic field changes associated with neuronal activity. Magnetic Resonance in Medicine. 2007; 57:411–416. [PubMed: 17260380]

Piechnik SK, Evans J, Bary LH, Wise RG, Jezzard P. Functional Changes in CSF Volume Estimated Using Measurement of Water T-2 Relaxation. Magnetic Resonance in Medicine. 2009; 61:579–586. [PubMed: 19132756]

Price DJ. Patterns of cytochrome oxidase activity in areas 17, 18, and 19 of the visual cortex of cats and kittens. Exp Brain Res. 1983; 58:125–133. [PubMed: 2985417]

Scouten A, Constable RT. VASO-based calculations of CBV change: accounting for the dynamic CSF volume. Magnetic Resonance in Medicine. 2008; 58:308–315. [PubMed: 18228581]

Strupp JP. Stimulate: A GUI based fMRI analysis software package. NeuroImage. 1996; 3:S607.

Tang L, Avison MJ, Gatenby JC, Gore JC. Failure to direct detect magnetic field-dephasing corresponding to ERP generation. Magnetic Resonance Imaging. 2008; 26:484–489. [PubMed: 18180125]

Tieman SB, Tumosa N. [^{14}C]-2-Deoxyglucose demonstration of the organization of ocular dominance in areas 17 and 18 of normal cat. Brain Res. 1983; 267:35–46. [PubMed: 6190537]

Trott O, Palmer AG. R-1 rho relaxation outside of the fast-exchange limit. Journal of Magnetic Resonance. 2002; 154:157–160. [PubMed: 11820837]

Truong TK, Song AW. Finding neuroelectric activity under magnetic-field oscillations (NAMO) with magnetic resonance imaging in vivo. Proceedings of the National Academy of Sciences of the United States of America. 2006; 103:12598–12601. [PubMed: 16894177]

van Zijl PCM, Yadav NN. Chemical Exchange Saturation Transfer (CEST): what is in a name and what isn't? Mag Reson Med. 2011; 65:927–948.

Xiong JH, Fox PT, Gao JH. Directly mapping magnetic field effects of neuronal activity by magnetic resonance imaging. Human Brain Mapping. 2003; 20:41–49. [PubMed: 12953305]

Xu, S.; Yang, J.; Shen, J. In vivo T1rho-weighted MR imaging of rat brain using a surface coil at 11.7T.. Proceedings of 16th ISMRM, Proceedings of 16th ISMRM; Toronto, Canada. 2008. p. 3077

Zhao F, Wang P, Hendrich K, Ugurbil K, Kim S-G. Cortical layer-dependent BOLD and CBV responses measured by spin-echo and gradient-echo fMRI: Insights into hemodynamic regulation. NeuroImage. 2006; 30:1149–1160. [PubMed: 16414284]

Zong X, Wang P, Kim S-G, Jin T. Sensitivity and Source of Amine-Proton Exchange and Amide-Proton Transfer Magnetic Resonance Imaging in Cerebral Ischemia. Magnetic Resonance in Medicine. 2013 DOI: 10.1002/mrm.24639.

Highlights

- Activation-induced change of $T_1\rho$ has both vascular- and tissue-originated components.
- $T_1\rho$ fMRI signal is dependent on magnetic field strength and spin-locking pulse parameters.
- Functional tissue $T_1\rho$ change shows distinct non-hemodyanmic characteristics.
- Tissue $T_1\rho$ fMRI signal may be caused by a change of metabolite concentration rather than pH.

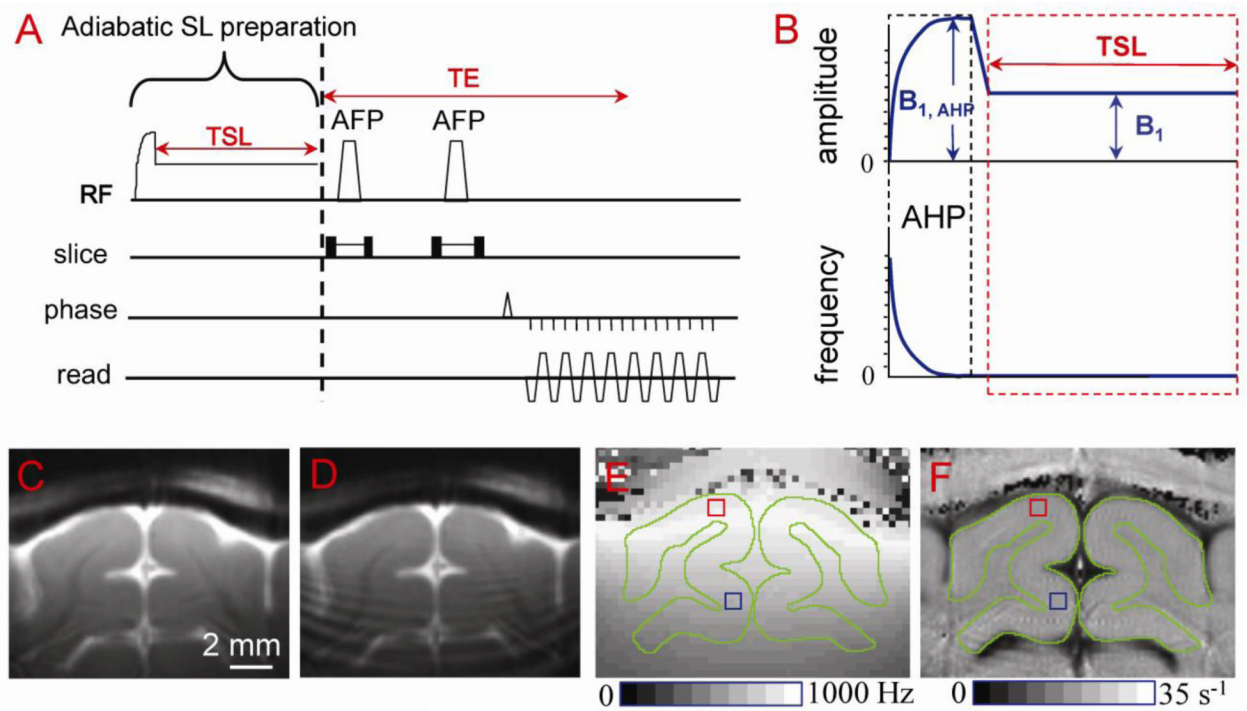

Fig. 1. Surface-coil $T_1\rho$ pulse sequence (A, B) and applications to cat primary visual cortex studies (C-F)

The pulse sequence (**A**) is a double spin-echo EPI acquisition with a non-selective spin-locking (SL) preparation (**B**). Adiabatic half passage (AHP, 2 ms in length with amplitude $B_{1,\,AHP}$) ensures that spins nutate into the transverse plane over a relatively large volume of B_1 inhomogeneity. The RF amplitude is then immediately ramped to the desired SL level (B_1) and held constant for the spin-lock time (TSL); the transmit frequency of the pulse remains the same during the short ramp and TSL. Following the spin-lock preparation, transverse spins are refocused by two adiabatic full-passage (AFP) pulses with slice-selection gradients. High quality $T_1\rho$-weighted image (ω_1 = 500 Hz and TSL = 40 ms) can be obtained when adiabatic SL condition is satisfied (**C**), but signal oscillations appear otherwise (**D**). (**E**) The spin-locking nutation frequency ω_1 map shows B_1 inhomogeneity. For our conditions, ω_1 at an area proximal to the coil (red square) is ~600 Hz, while at a distal area (blue square) it is ~ 400 Hz. Gray matter areas are outlined in green. (**F**) The map of $R_1\rho$ (=$1/T_1\rho$) shows little spatial variations within visual cortex because the $T_1\rho$ dispersion is very small within the narrow ω_1 range (e.g., 400-600 Hz).

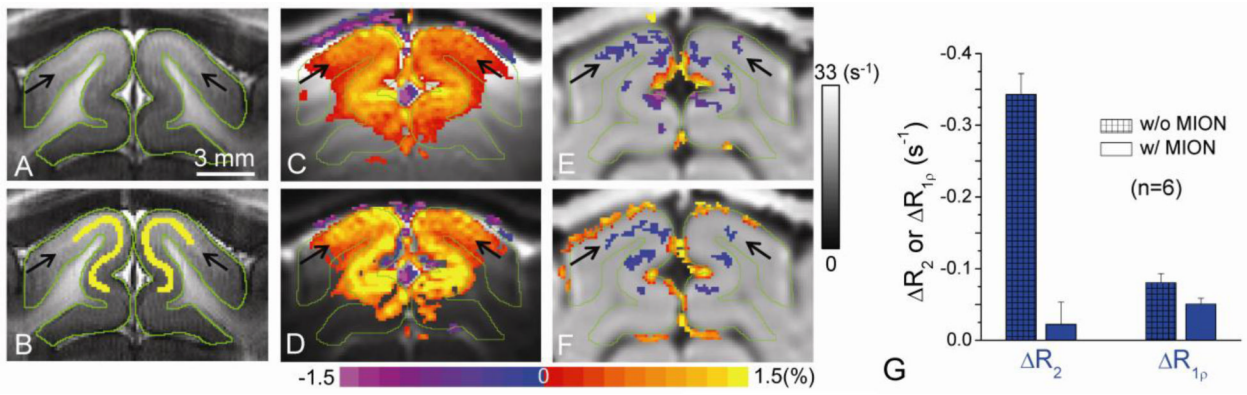

Fig. 2. Intravascular and extravascular contributions to functional $R_1\rho$ change in the cat visual cortex

A slightly bright band (indicated by black arrows) within the gray matter (outlined in green) in high-resolution T_1-weighted EPI image (**A**) indicates cortical layer IV (Kim and Kim, 2011). Pixels along the white band (yellow) were chosen for quantitative analyses of cat's functional studies (**B**). All active pixels were overlaid in color on their respective baseline images (**C-F**), and the vertical grayscale bar indicates the baseline $R_1\rho$ values (for **E** and **F**). Functional percentage signal change maps were obtained by T_2-weighted (TSL = 0, **C**) and $T_1\rho$-weighted fMRI (TSL = 50 ms and ω_1 = ~500 Hz, **D**) without MION during visual stimulation. Higher changes were observed in $T_1\rho$-weighted fMRI, indicating an increase in $T_1\rho$ (decrease in $R_1\rho$). To determine the blood contribution, $R_1\rho$ change maps obtained without (**E**) and with (**F**) 5 mg/kg MION were compared. An increase in $R_1\rho$ at the surface of the cortex is due to a volume fraction change between tissue and CSF, while a decrease in $R_1\rho$ is located at the middle of the cortex. (**G**) At the middle cortical ROI (yellow pixels in **B**), the functional R_2 change (ΔR_2) is nearly suppressed with MION injection, whereas $\Delta R_1\rho$ only decreases slightly.

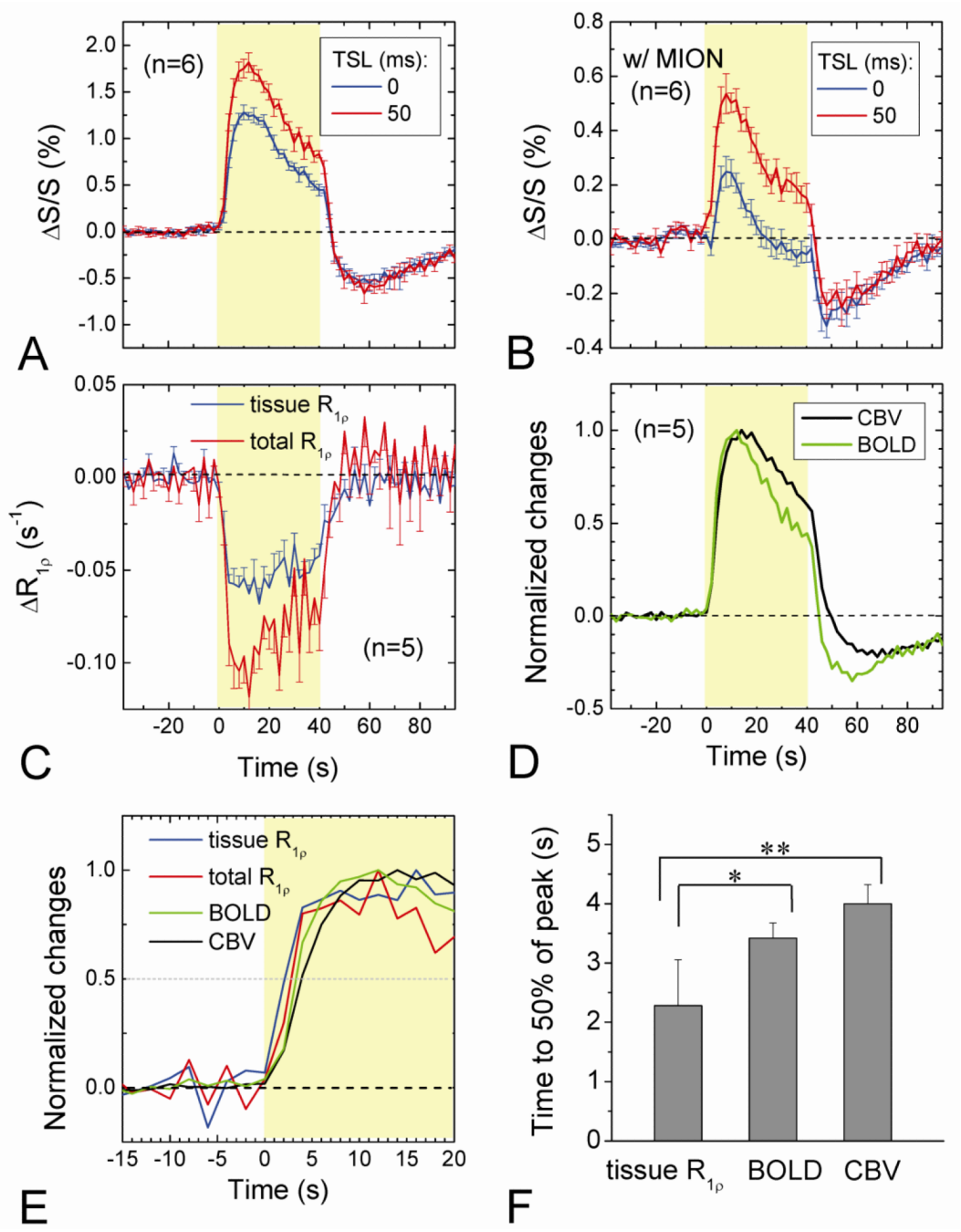

Fig. 3. Dynamic changes in BOLD, $T_1\rho$-weighted fMRI, CBV, and $R_1\rho$ without and with MION during visual stimulation

Averaged time courses of T_2-weighted (TSL = 0), $T_1\rho$-weighted fMRI (TSL = 50 ms), and $R_1\rho$ change were obtained from the middle cortical ROI during visual stimulation without and with blood signal suppression with MION (**A-C**). The normalized time courses of BOLD and CBV show a significant undershoot after the stimulus offset (**D**), unlike those time courses of the two $R_1\rho$ responses (**C**). The BOLD, CBV, total $R_1\rho$ (without MION) and tissue $R_1\rho$ responses were normalized and their initial rising periods during stimulation were compared in (**E**). The rising time, defined as the time from the stimulus onset to 50%

of the peak change, is faster for the tissue $R_1\rho$ than BOLD ($p < 0.05$, $n = 5$) and CBV ($p < 0.01$) responses (**F**).

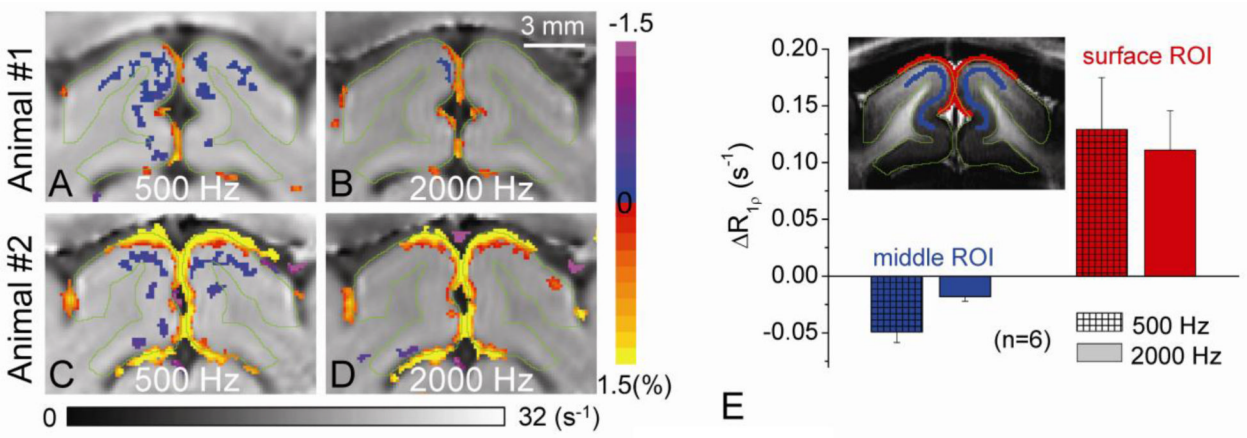

Fig 4. Functional tissue $R_1\rho$ changes at two spin-locking frequencies

Visual stimulation-induced tissue $R_1\rho$ changes were measured after 5 mg/kg MION for two SL frequencies ω_1 = 500 and 2000 Hz. Tissue $R_1\rho$ change maps of two representative animals were shown for ω_1 = 500 Hz (**A, C**) and 2000 Hz (**B, D**), where the horizontal grayscale bar indicates the baseline $R_1\rho$ values and the vertical color bar indicates the functional change. The $R_1\rho$ decrease at the parenchyma is significantly reduced for ω_1 = 2000 Hz, whereas the $R_1\rho$ increasing pixels at the surface of the cortex are similar for the two frequencies. The averaged change (n = 6 cats) in tissue $R_1\rho$ at ω_1 = 500 Hz is 2.7 times larger than that at 2000 Hz (**E**).

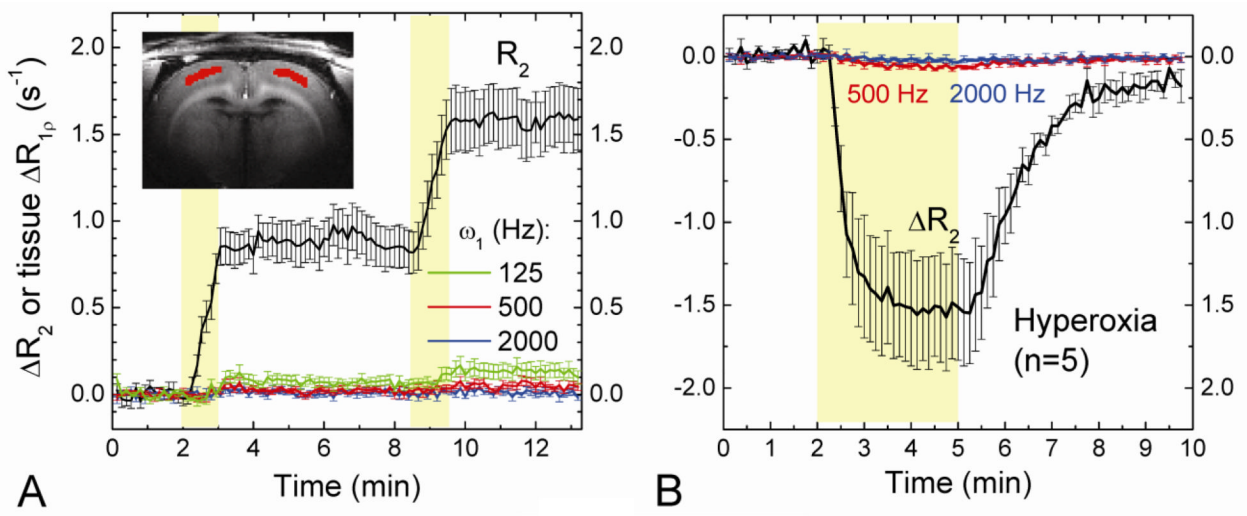

Fig. 5. Effects of intravascular susceptibility variation and hyperoxia challenge on extravascular water $R_1\rho$

In order to detect the contribution of intravascular susceptibility changes to tissue $R_1\rho$, the blood signal was suppressed with the injection of 5 mg/kg MION before experiments. Dynamic changes in tissue R_2 and $R_1\rho$ were obtained during two injections of 1 mg/kg MION (**A**, n = 4 rats) and 3 minutes inhalation of 60% O_2 (**B**, n = 5 rats) indicated by the yellow shaded regions. Time courses were obtained from the red pixels within the cortex (Inset). When spin-locking frequencies were measured at ≥500 Hz, a variation in intravascular susceptibility does not contribute to tissue $R_1\rho$ measurements.

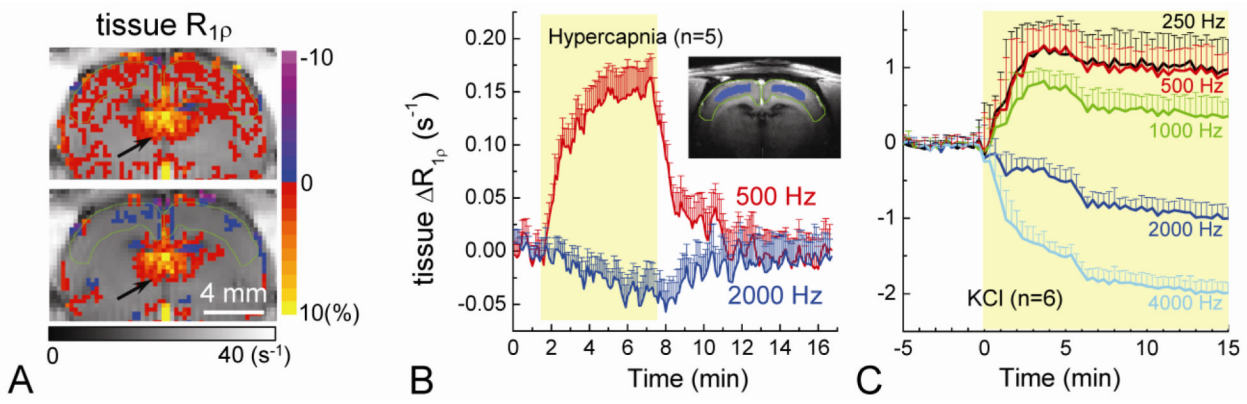

Fig. 6. Spin-locking frequency-dependent tissue $R_{1\rho}$ change during tissue acidosis

Tissue $R_{1\rho}$ changes were measured during hypercapnia and global ischemia after 5 mg/kg MION injection. Tissue $R_{1\rho}$ change maps for ω_1 = 500 Hz and 2000 Hz are shown for hypercapnic challenge in one rat (**A**). Green contour indicates the cortical area. Unlike visual stimulation, an increase in tissue $R_{1\rho}$ was observed for ω_1 = 500 Hz. Note that the increases of $R_{1\rho}$ near the ventricle area are similar in the two maps and can be attributed to a change of CSF volume fraction (arrows). The averaged time course (n = 5 rats) of the tissue $R_{1\rho}$ response obtained the cortical ROI (**Inset**) shows a significant increase for 500 Hz whereas a small decrease for 2000 Hz (**B**). The averaged tissue $R_{1\rho}$ responses (n = 6 rats) for ω_1 from 250 to 4000 Hz during KCl injection (**C**), which induces tissue acidosis, show spin-locking frequency-dependent changes. These are qualitatively similar to hypercapnia.

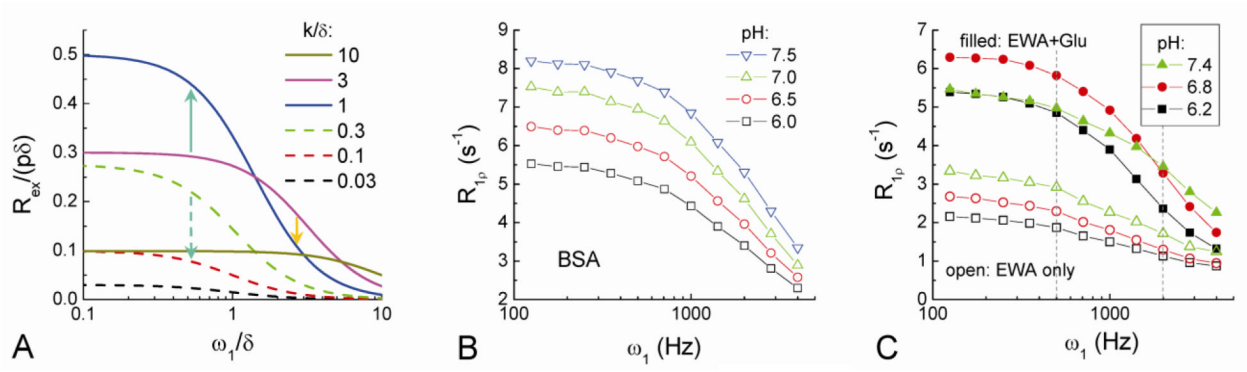

Fig. 7. Calculated R_{ex} dispersion (A) and the measured $R_1\rho$ dispersion of pH-dependent phantoms (B-C)

R_{ex} dispersion was calculated with Eq. [4] as a function of exchange rate *k*. Upward and downward arrows indicate changes in R_{ex} when the exchange between labile protons and water is slow down due to pH decrease (see texts). The $R_1\rho$ dispersion of 8% bovine serum albumin (BSA) decreases with pH values (**B**). The $R_1\rho$ dispersion of 4% egg white albumin (EWA) only (open symbols) and 4% EWA with 30 mM of glutamate (filled symbols) were both measured for three pH values (**C**). Vertical dashed lines (C) indicate spin-locking frequencies of 500 and 2000 Hz used for *in vivo* studies. The addition of glutamate (Glu) changes the pH-dependence of $R_1\rho$ dispersion.

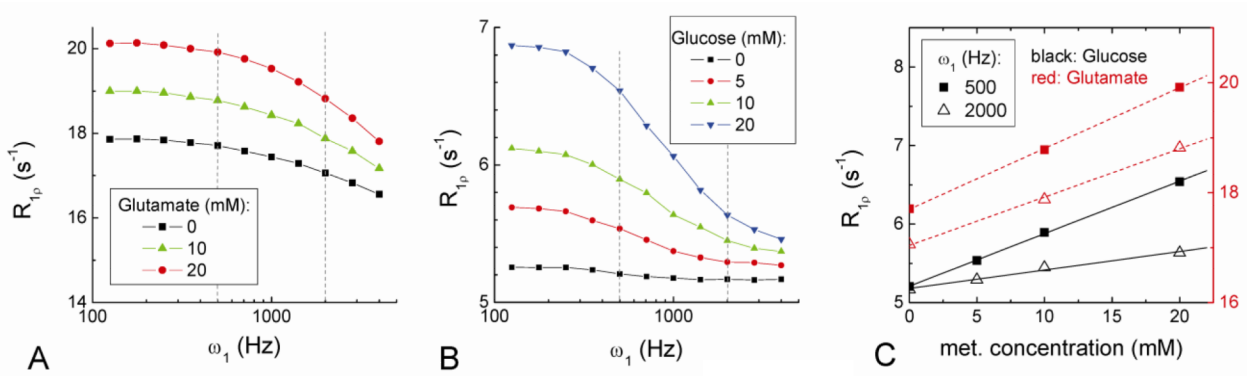

Fig. 8. $R_1\rho$ dispersions of concentration-dependent amine and hydroxyl metabolite phantoms

Three amine-containing glutamate concentrations in agarose with 0.07 mM $MnCl_2$ (**A**), and four hydroxyl-containing glucose (Glc) concentrations in PBS with 0.1 mM $MnCl_2$ (**B**) were used. $R_1\rho$ is linearly dependent on Glu and Glc concentration, and the slope for ω_1 = 500 Hz is only slightly larger than that for ω_1 = 2000 Hz for Glu, but is much larger for Glc (**C**). The ratio of $R_1\rho$ at ω_1 = 500 Hz to 2000 Hz is similar for glucose phantom (2.8) and for *in vivo* functional response (2.7).